




**Strong renormalization of Ba vibrations in thermoelectric type-IX clathrate Ba<sub>24</sub>Ge<sub>100</sub>**R. Viennois <sup>1,\*</sup>, M. Beauduin <sup>1</sup> and M. M. Koza <sup>2</sup><sup>1</sup>*ICGM, Univ Montpellier, CNRS, ENSCM, Montpellier, France*<sup>2</sup>*Institut Laue Langevin, 71 Avenue des Martyrs, CS 20156, F-38042 Grenoble, France*

(Received 10 December 2021; revised 24 January 2022; accepted 28 January 2022; published 23 February 2022)

We report a combined experimental and theoretical study of the lattice dynamics of the type IX clathrate Ba<sub>24</sub>Ge<sub>100</sub> by inelastic neutron scattering (INS) experiments and density functional theory (DFT) calculations. We observe low-energy optical modes at  $\sim 2\text{--}3\text{ meV}$  due to the motion of the heavy Ba atoms along the high-symmetry axis and the largest dimension of the open Ge@20 cages present in the compound. Even though the phonon participation ratio indicates that these low-energy modes are localized, their  $Q$  dependence shows that the dynamics of the Ba guests are correlated. We observe a strong change in the spectral weight of these modes when the compound undergoes a temperature-induced structural transformation in the temperature range 190–230 K. In the high-temperature phase, the low-energy optical modes show high intensities in the INS data and frequencies rather insensitive to temperature changes up to  $\sim 550\text{ K}$ . In the low-temperature structural modification, the low-energy mode intensities are strongly depleted and apparently shifted to higher energies; this behavior is in line with an off-centering of the Ba atoms at low temperatures. Our DFT calculations successfully approximate the essential features in the dynamics of the high-temperature Ba<sub>24</sub>Ge<sub>100</sub> structure.

DOI: [10.1103/PhysRevB.105.054314](https://doi.org/10.1103/PhysRevB.105.054314)**I. INTRODUCTION**

The study of thermoelectric materials is a growing field due to the emergency to find environmentally friendly energy sources. The efficiency of thermoelectric materials is represented by the dimensionless figure of merit  $ZT = S^2\sigma T/\lambda$ , with  $S$  the Seebeck coefficient,  $\sigma$  the electrical conductivity,  $\lambda$  the thermal conductivity, and  $T$  the absolute temperature. To reach high efficiencies, thermoelectric materials need to be poor thermal conductors, thus to exhibit a  $\lambda$  as low as possible [1].

During the last two decades, thermoelectric materials were found showing advanced efficiencies for high-temperature thermoelectric applications. The reduced  $\lambda$  was accomplished by following some simple concepts such as the phonon glass electron crystal (PGEC) idea proposed by Slack [2]. Cage compounds such as clathrates and filled skutterudites are groups of structurally complex compounds to which the PGEC concept was applied with great success [3,4]. However, to date, the origin of the microscopic mechanism behind the low thermal conductivity is disputed, although it is clearly related to the vibrations of the atoms intercalated within the spacious cages of these cage compounds.

In the past, it was proposed that phonon Umklapp scattering was enhanced in filled skutterudites because of additional scattering channels for heat-carrying acoustic phonons introduced by the presence of low-lying optical modes. The low-energy optical modes involve mainly motions of heavy rare-earth atoms intercalated in the spacious cages [5].

Later, our experimental studies supported this scenario by careful measurements of phonon density of states (DOS) of

filled  $R\text{Fe}_4\text{Sb}_{12}$  ( $R = \text{La}, \text{Ce}$ ) skutterudites [6] as well as phonon dispersion of  $\text{LaFe}_4\text{Sb}_{12}$  [7] and showed that the low-lying optical modes were strongly harmonic, which contrasts the resonant scattering scenario proposed in the “rattling” picture. We also found similar behavior in the metastable type-I Ba<sub>8</sub>Si<sub>46</sub> clathrate, which contains two types of cages [8]. However, in some other cage compounds such as osmate pyrochlore [9],  $R\text{V}_2\text{Al}_{20}$  with  $R = \text{Al}, \text{Ga}$  [10], or type-VIII Ba<sub>8</sub>Ga<sub>16</sub>Sn clathrate [11], a large anharmonicity was found for the low-lying optical modes involving mainly motions of the intercalated atoms.

We recently investigated the metastable type-IX chiral cubic Ba<sub>24</sub>Si<sub>100</sub> clathrate, which contains three types of cages and has no equivalent counterpart among hydrate or silicate clathrates. In this structure, 8 Ba1 atoms are located in closed Si@20 cages, 4 Ba2 atoms are located in distorted cubic Si@8 cages, and 12 Ba3 atoms are located in open Si@20 cages. We found significant anharmonicity for the vibrations of the Ba atoms along the larger dimensions of the large open Si@20 cages with energies as low as 2–3 meV [12]. There exist other type-IX clathrates such as Ba<sub>24</sub>Ge<sub>100</sub>, having the advantage of being thermodynamically stable [13–15]. This compound has very interesting properties such as superconductivity at low temperature and first-order metal-semiconductor transition which is accompanied by a temperature-induced structural transformation in the 150–250 K temperature range whose origin is still under discussion [13–20]. The low-temperature phase has the same space group as the room-temperature phase, but the Ba atoms located in the distorted cubic Ge@8 interstices and in the open Ge@20 cages become locked in at split sites [17–20].

The electronic structures of both room- and low-temperature phases were studied by density functional theory

\*Corresponding author: [romain.viennois@umontpellier.fr](mailto:romain.viennois@umontpellier.fr)

(DFT) calculations [21,22] as well as by x-ray photoemission spectroscopy [23,24]. A strong decrease of the DOS at the Fermi level was observed in the low-temperature phase [23,24] and confirmed by nuclear magnetic resonance experiments [25,26]. Diffraction studies also indicate an anomalous behavior of the thermal expansion in the region of the structure transformation: the thermal expansion becomes negative in the 190–230 K temperature range [19,20]. These studies also indicate an increase of the anisotropy of the charge density of the Ba atoms intercalated in the open Ge@20 cages during the phase transition, pointing to the essential role played by their vibrations during the temperature-induced structure transformation [19,20].

When high pressure is applied on Ba<sub>24</sub>Ge<sub>100</sub>, the temperature of the metal-semiconductor transition decreases and eventually disappears at 2.8 GPa [16]. At the same time, the superconducting temperature is 16-fold enhanced, mainly by the increase of the DOS at the Fermi level [16,27]. The metal-semiconductor transition temperature also decreases when Ba<sub>24</sub>Ge<sub>100</sub> is alloyed with Eu or Na on the Ba site and even disappears when one third of Ba is replaced by Na [16,17]. Interestingly, when the Ge site is substituted by an element of the third column, the structure transformation temperature is lowered. One also notices that the thermal conductivity decreases to  $\sim 0.8$  W/mK for Ba<sub>24</sub>Ga<sub>15</sub>Ge<sub>85-x</sub> which is a very good thermoelectric material with  $ZT$  reaching a value as high as 1.3 at  $\sim 680$  °C [28–30].

The above results call for a thorough investigation of the lattice dynamics (LD) of Ba<sub>24</sub>Ge<sub>100</sub>, especially to understand the role played by the dynamics of the guest atoms in the structural transition observed in the parent compound Ba<sub>24</sub>Ge<sub>100</sub> and to comprehend the origin of the low thermal conductivity induced by a substitution on the Ge sites. Although these compounds have very interesting properties, LD studies at low  $T$  are lacking; only a Raman study under high pressure (up to 26 GPa) has been reported [31]. Neither inelastic neutron scattering (INS) experiments monitoring the vibrational properties nor *ab initio* DFT calculations of the LD of these compounds have been reported.

In this paper, we report on the LD of the type-IX clathrate Ba<sub>24</sub>Ge<sub>100</sub>. We first report a combined study of the harmonic properties and LD of Ba<sub>24</sub>Ge<sub>100</sub> with DFT calculations and spectroscopic tools such as INS experiments. We then report on the INS experiments as a function of temperature to probe the changes induced by the phase transition in the LD as well as the anharmonicity. DFT calculations of the atomic potential of the different guest atoms were carried out to study the guest dynamics and their anharmonicity. High temperature x-ray diffraction (XRD) experiments were performed for determining the thermal expansion and Grüneisen parameter in the high-temperature phase.

## II. EXPERIMENTAL AND COMPUTATIONAL DETAILS

### A. Sample synthesis and characterization

Polycrystalline samples of Ba<sub>24</sub>Ge<sub>100</sub> were prepared by arc melting of Ba (98.5% lump) and Ge (99.999% lump) and found to be single-phase Ba<sub>24</sub>Ge<sub>100</sub> as evidenced by XRD experiments. The quality of the samples is documented in

Appendix A. The specimens were analyzed after synthesis at room temperature by using an XRD apparatus (Philips X'PERT PRO II with Cu K  $\alpha_1$  and K  $\alpha_2$  radiations). Rietveld refinement with FULLPROF software was applied for the structural analysis [32]. We found a lattice parameter  $a = 14.5566(1)$  Å ( $\chi^2 = 10.9$ ,  $R_{\text{Bragg}} = 8.57$ ,  $R_F = 5.36$ ) in good agreement with prior experimental works. The corresponding fractional atomic positions and isotropic atomic displacement parameters (ADPs) are reported in Table I. The high-temperature XRD experiments were performed using an XRD apparatus (Empyrean with Co K  $\alpha_1$  and K  $\alpha_2$  radiations) and a heater made of Ta under secondary vacuum. The lattice parameters were determined using pattern matching with FULLPROF software [32]. The results are depicted in Appendix A [Fig. 11(a)]. To determine the characteristic temperatures of the metal-insulator and structural transitions, we have carried out magnetic susceptibility experiments under an external magnetic field of 1 T using a superconducting quantum interference device magnetic properties measurements system apparatus from Quantum Design. The results are reported in Appendix A [Fig. 11(b)]. Our results agree well with those of Paschen *et al.* [17].

### B. INS experiments

High-resolution INS experiments were performed with the cold-neutron time-of-flight spectrometers IN5 and IN6 at the Institut Laue Langevin in Grenoble, France. The IN5 spectrometer was utilized with the incident wavelengths of 1.8, 2.5, and 5 Å, resulting in an elastic energy resolution of 1.5, 0.6, and 0.08 meV, respectively. A wavelength of 4.14 Å with an elastic resolution of 0.17 meV was utilized at the IN6 spectrometer. Basic corrections were applied to the recorded data comprising empty holder scattering, frame overlap, and instrument background signals, scaling for different detector efficiencies as well as its energy dependence. The signal was transformed afterward to the dynamical structure factor applying established mathematical relations. The generalized DOS (GDOS) was computed within the incoherent approximation for coherently scattering materials similarly to a recent approach performed for skutterudites and Ba-Ge clathrates [33–36]. As Ba and Ge atoms are rather weak neutron scatterers, the signal of the sample was low, even with  $\sim 7$  g of sample material, which makes the determination of the  $Q$  dependence of the dynamical structure factor challenging.

### C. *Ab initio* and LD calculations

LD calculations were carried out with the direct method from the Hellmann-Feynman (HF) forces computed on the relaxed clathrate structures with the Vienna *Ab initio* Software Package (VASP). The DFT calculation was based on projector augmented wave pseudopotentials and the PBE exchange-correlation functional [37,38]. We have used the finite-temperature smearing first-order Methfessel-Paxton method for the band occupancies [39]. For all calculations, an energy cutoff of 350 eV, an energy convergence of  $10^{-10}$  eV, and a force convergence of  $10^{-4}$  eV/Å were applied with a Monkhorst-Pack [40] k-mesh of  $5 \times 5 \times 5$ . Detailed information about the relaxed atomic positions and displacement

TABLE I. Atomic positions and isotropic ADPs of Ba<sub>24</sub>Ge<sub>100</sub> at room temperature from Rietveld refinement of XRD data (left) and from DFT calculations (right).

Atom	Wyckoff	$x$	$y$	$z$	$U_{\text{iso}}$	$x$	$y$	$z$	$U_{\text{iso}}$
Ba1	8c	0.1894(2)	$x$	$x$	0.007(1)	0.192	$x$	$x$	0.0157
Ba2	4b	$\frac{7}{8}$	$x$	$x$	0.023(2)	$\frac{7}{8}$	$x$	$x$	0.0277
Ba3	12d	$\frac{1}{8}$	0.8102(2)	$y + 0.25$	0.045(2)	$\frac{1}{8}$	0.8115	$y + 0.25$	0.064
Ge1	8c	0.0287(3)	$x$	$x$	0.026(3)	0.0315	$x$	$x$	0.026
Ge2	24e	0.2015(3)	0.0426(3)	0.0004(3)	0.013(2)	0.2041	0.0424	0.0017	0.017
Ge3	12d	$\frac{1}{8}$	0.1700(3)	$y + 0.25$	0.013(2)	$\frac{1}{8}$	0.1711	$y + 0.25$	0.018
Ge4	24e	0.2395(3)	0.9338(3)	0.8758(3)	0.012(1)	0.2391	0.9331	0.8756	0.018
Ge5	24e	0.4169(3)	0.8526(3)	0.0835(3)	0.009(1)	0.4167	0.8519	0.0851	0.020
Ge6	8c	0.3267(3)	$x$	$x$	0.008(3)	0.3256	$x$	$x$	0.017

parameters is offered in Table I. The relaxed lattice parameter found is 14.8636 Å and is by  $\sim 2\%$  larger than the experimental values (14.55–14.56 Å) which is typical of the PBE exchange-correlation functional [41]. We have also calculated the variation of the energy as a function of the volume and from fitting with the Vinet equation [42] and found the bulk modulus  $B = 37.5$  GPa and its pressure derivative  $dB/dP = 4.75$ . These values are smaller than the experimental values found by Yuan *et al.* [27]:  $B = 44(2)$  GPa and  $dB/dP = 5.8(8)$ . The electronic DOS is reported in Appendix B and is in very good agreement with the calculations of Zerec *et al.* [21].

The HF forces were derived by displacing atoms from their equilibrium positions by 0.03 Å along nonequivalent high-symmetry directions. For the equilibrium configuration, the atom positions were relaxed with a force convergence of  $10^{-4}$  eV/Å. The LD properties were computed from the HF forces by the diagonalization of the dynamical matrix with the software package PHONON [43]. For a better comparison of the GDOS with the DFT results, the neutron-weighted phonon DOS  $Z'(E)$  was calculated using  $Z'(E) = \sum_i \frac{\sigma_i}{M_i} Z_i(E)$ , where  $Z_i(E)$  are the atom-projected DOS,  $\sigma_i$  are the scattering cross-sections, and  $M_i$  are the atom masses of each atom. For convenience,  $Z'(E)$  was broadened by a Gaussian for better comparison with the experimental data.

The ADPs were computed in harmonic approximation [44]. The participation ratio  $p(\omega)$  describes the degree of participation of the different atoms to a particular vibrational eigenstate [12,45,46]. It has been extracted from the above calculations using [12,45,46]

$$p(\omega) = \frac{\left( \sum_{i=1}^N |\tilde{u}_i(\omega_{\vec{q}})|^2 \right)^2}{N \sum_{i=1}^N |\tilde{u}_i(\omega_{\vec{q}})|^4}, \quad (1)$$

where  $\tilde{u}_i = \vec{e}_i(\vec{q})/\sqrt{M_i}$  are the atomic amplitudes with the phonon polarization vector  $\vec{e}_i(\vec{q})$  and the mass  $M_i$  of atom  $i$ .

The calculations of the atomic potential as a function of the displacements of the Ba guest atoms  $\Delta x$  have been performed in the same conditions as the calculations of the HF forces.

### III. RESULTS

The clathrate Ba<sub>24</sub>Ge<sub>100</sub> crystallizes in the noncentrosymmetric chiral cubic structure of space group  $P4_132$  (number 213) with 124 atoms in the primitive cell. Thus, there are 372 vibrational eigenmodes. Their irreducible representation at the Brillouin zone center is determined by the group theory to

$$\Gamma_{\text{opt}} = 14 A_1 \oplus 17 A_2 \oplus 31 E \oplus 47 T_1 \oplus 45 T_2$$

and  $\Gamma_{\text{ac}} = T_1$ ,

where the  $A$ ,  $E$ , and  $T$  modes are respectively singly, doubly, and triply degenerate. Thus, there are 90 different frequencies associated with Raman-active modes of  $A_1$ ,  $E$ , and  $T_2$  symmetry and 47 different frequencies from infrared-active modes of  $T_1$  symmetry. We present in Fig. 1 the vibrational DOS and the full set of Raman-active  $\Gamma$ -point eigenfrequencies computed from DFT calculations. The complete set of  $\Gamma$ -point eigenfrequencies and their symmetries are listed in Appendix B. In Fig. 2, we compare the computed neutron-weighted phonon

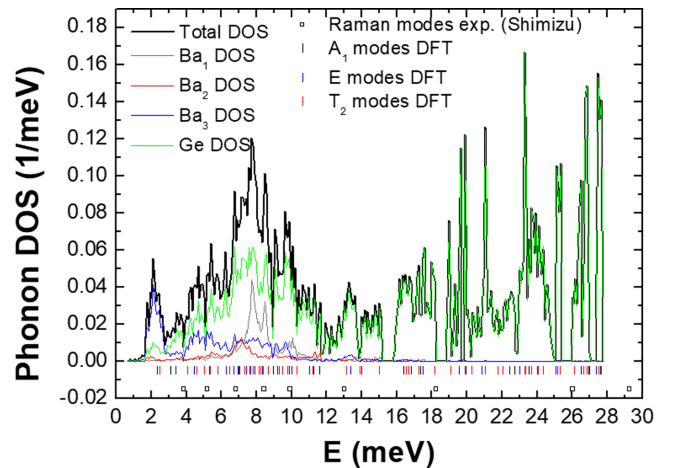


FIG. 1. Total and atom-projected phonon density of states (DOS) of Ba<sub>24</sub>Ge<sub>100</sub> obtained from density functional theory (DFT) calculations. Contribution from Ba is discriminated according to their Wyckhoff positions. Vertical bars indicate computed  $\Gamma$ -point eigenfrequencies; open squares report Raman frequencies measured by Shimizu *et al.* [31].



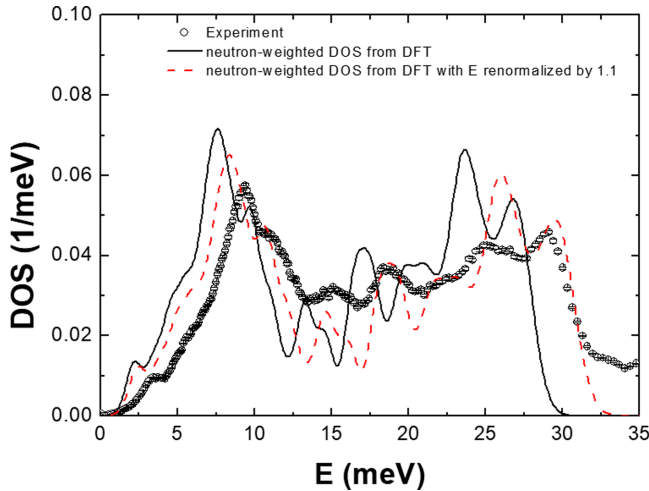


FIG. 2. Generalized density of states (GDOS) of  $\text{Ba}_{24}\text{Ge}_{100}$  (empty circles) measured on IN5 at 300 K with 5 Å and neutron-weighted DOS  $Z'(E)$  (black solid lines) computed from density functional theory (DFT) results and convoluted with a Gaussian mimicking the IN5 energy resolution. Red dashed line corresponds to  $Z'(E)$  data with energies renormalized by a factor 1.1 to match the position of the highest energy peak.

DOS  $Z'(E)$  with the GDOS derived from an INS experiment with 5 Å at 300 K.

As shown in Fig. 2, the measured GDOS of  $\text{Ba}_{24}\text{Ge}_{100}$  extends up to an energy of  $\sim 34$  meV and is characterized by a strong peak  $\sim 10$  meV and an overall rich texture indicating localized excitations down to  $< 4$  meV. A similar behavior has been observed in the two other binary compounds  $\text{Ba}_8\text{Ge}_{43}$  and  $\text{BaGe}_5$  despite their structural and stoichiometric differences [34,47]. It can be judged from the atom-projected DOS presented in Fig. 1 that the low-energy range of excitations is influenced by Ba amplitudes, whereas the high-energy spectral density is dominated by the Ge signal. The details of the atom-projected DOS of the different Ge atoms are given in Appendix B.

Comparing the present data to the dynamics of the isostructural  $\text{Ba}_{24}\text{Si}_{100}$  [8,12], the coupling of Ba to the different host networks becomes obvious by the shift of the dominating low-energy peak from 10 to 20 meV, and the specifics of the host dynamics are highlighted by the shift of the spectral cutoff to  $> 52$  meV in  $\text{Ba}_{24}\text{Si}_{100}$  [12].

Our LD calculations of  $\text{Ba}_{24}\text{Ge}_{100}$  show that the energies of the vibrational modes extend up to  $\sim 30$  meV. Thus, the DFT calculations underestimate the phonon energies similarly as observed for the cases of  $\text{Ba}_8\text{Ge}_{43}$  [34] and  $\text{Ba}_{24}\text{Si}_{100}$  [12]. This is in line with the overestimation of the lattice parameters using the PBE exchange-correlation functional, as we indicate below. However, the neutron-weighted  $Z'(E)$  shown in Fig. 2 can reproduce all spectral features identified by the INS experiments. To account for the energy mismatch, we also report  $Z'(E)$  with energies renormalized by a factor 1.1. In this case, we observe good agreement of the different spectral features  $> 13$  meV, thus for the Ge-dominated vibrations. Nonetheless, there is still disagreement for Ba-influenced excitations  $< 13$  meV and especially for the peak of lowest energy whose

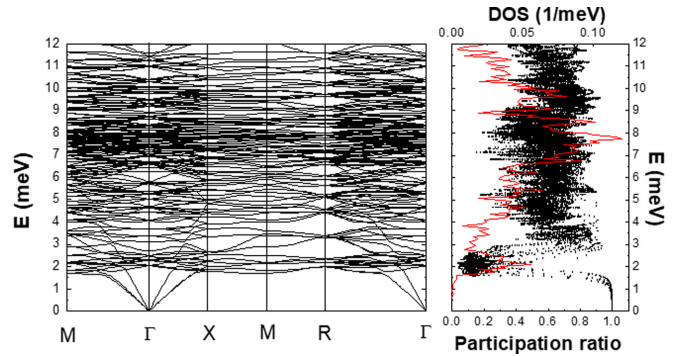


FIG. 3. (left) Phonon dispersion and (right) participation ratios of  $\text{Ba}_{24}\text{Ge}_{100}$  based on density functional theory (DFT) calculations. For clarity, the corresponding phonon density of states (DOS) is reported in red with the participation ratio.

characteristic frequency we identify to  $\sim 2.2$  meV in the DFT calculations and to 3.3 meV in the experiments. Despite the energy mismatch of our calculation, all computed features agree well with the experiment data on a qualitative basis.

In a recent extensive DFT work, Euchner and Groß [48] addressed and detailed the phonon renormalization problem by different exchange-correlation functionals for the specific example of type-I Ba-Ge clathrates. They have demonstrated that, among others comprising PBE, the meta-GGA SCAN exchange-correlation functional approximates experimental

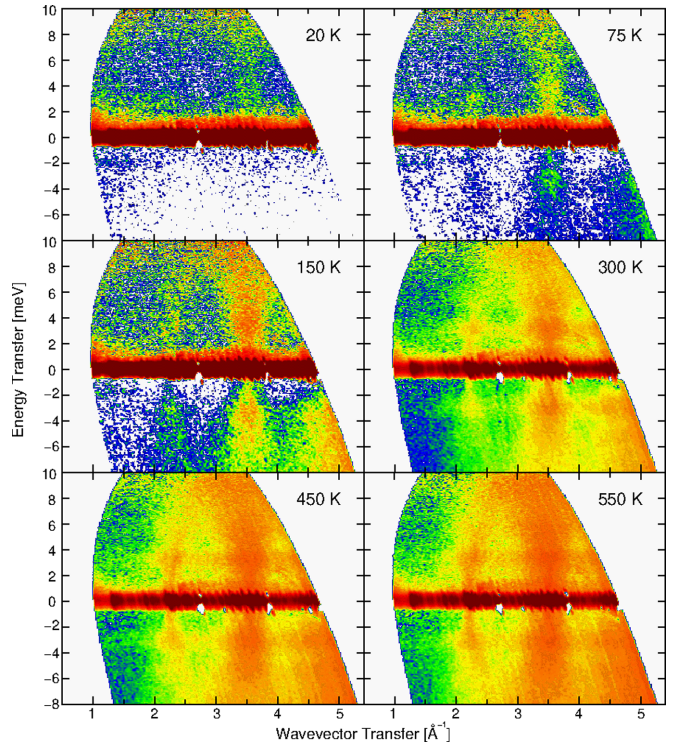


FIG. 4. Intensity maps of the dynamic structure factor of  $\text{Ba}_{24}\text{Ge}_{100}$  measured on IN5 with an incident wavelength of 2.5 Å at the indicated temperatures. Note the strong dispersionless excitation band centered at  $\sim 3.3$  meV formed at  $T$  above the structural transformation at 190–230 K.

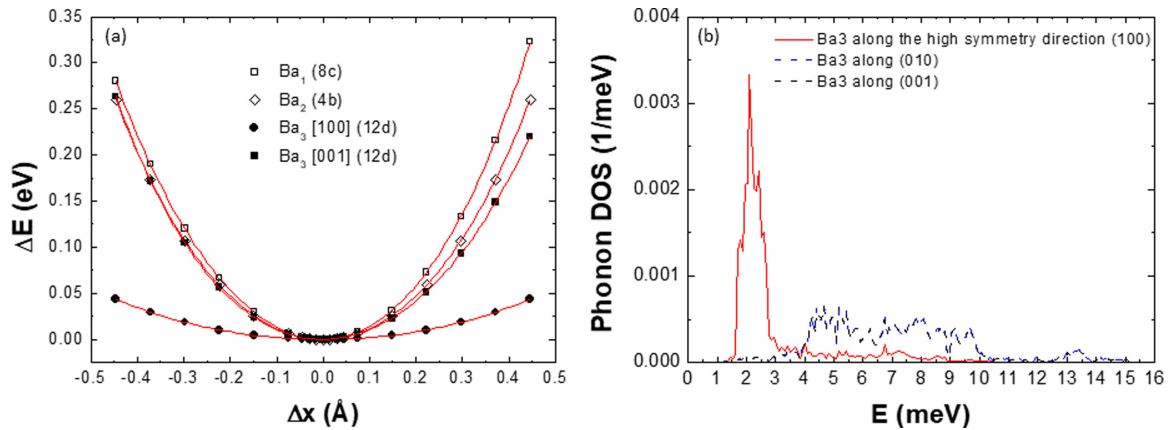


FIG. 5. (a) Density functional theory (DFT) calculated atomic potentials  $\Delta E$  vs  $\Delta x$  displacement of the Ba atoms in  $\text{Ba}_{24}\text{Ge}_{100}$ . The red solid lines represent results from a polynomial fit of fourth order. (b) Directional atom-projected phonon densities of states of the Ba3 atom of  $\text{Ba}_{24}\text{Ge}_{100}$  obtained from DFT calculations.

data best. Such a detailed approach is beyond the scope of this paper.

A congruent conclusion upon underestimation of eigenfrequencies by the PBE functionals can be drawn comparing our DFT data with results from Raman scattering experiments by Shimizu *et al.* [31], both reported in Fig. 1. The experimental Raman spectrum of Shimizu *et al.* [31] extends from 3.85 meV ( $31\text{ cm}^{-1}$ ) to 29.25 meV ( $236\text{ cm}^{-1}$ ) and is upshifted compared with the DFT calculations. Examining the experimental data only, we see that the lowest energy Raman mode at 3.85 meV [31] matches well with the position of the first peak in our INS GDOS data, see Fig. 2. We note that, in our DFT data, several modes with different symmetries contribute to each of the resolution-limited peaks in the INS data. It is therefore impossible to make an unambiguous assignment of specific Raman-active modes to these peaks.

We disclose the low-energy inelastic properties of  $\text{Ba}_{24}\text{Ge}_{100}$  in more detail by reporting in Fig. 3 the DFT-computed phonon dispersion and participation ratios  $<12\text{ meV}$ . As evidenced by the phonon dispersion, there is a high number of dispersionless, localized phonons contributing to the peak of lowest energy  $\sim 2.2\text{ meV}$ . Thus, the intensity

of this peak in the DOS is as well formed by vibrational eigenstates away from the  $\Gamma$  point. The localized character of these eigenstates is expressed by their low participation ratio reported on the right-hand side of Fig. 3. Like the isostructural  $\text{Ba}_{24}\text{Si}_{100}$  [12] compound, the participation ratio takes on numbers as low as 0.037 around the center of the 2.2 meV peak. Another notable point is the position of this peak in comparison with data measured and computed for other Ba-Ge clathrates. We notice that it takes on the lowest value when compared with results of the binary  $\text{Ba}_8\text{Ge}_{43}$  [34],  $\text{BaGe}_5$  [47], and ternary  $\text{Ba}_8\text{Ge}_{46-x}\text{M}_x$  ( $M = \text{Zn, Pd, Au, Ga}$ ) [34,49–52] compounds.

The contribution of noncenter eigenstates of an energy as low as 2.2 meV manifests itself in a strong dispersionless mode band in the experimental data at 3.3 meV. We demonstrate its existence in Fig. 4 with spectra recorded at IN5 with 2.5 Å incident wavelength and different temperatures. Additional density maps recorded at IN5 with 1.8 Å incident wavelength and different temperatures are plotted in Appendix C. Above the temperature range of structural transformation (190–230 K), a band of strong intensity centered at  $\sim 3.3\text{ meV}$  is observable throughout the entire  $Q$  range. In all

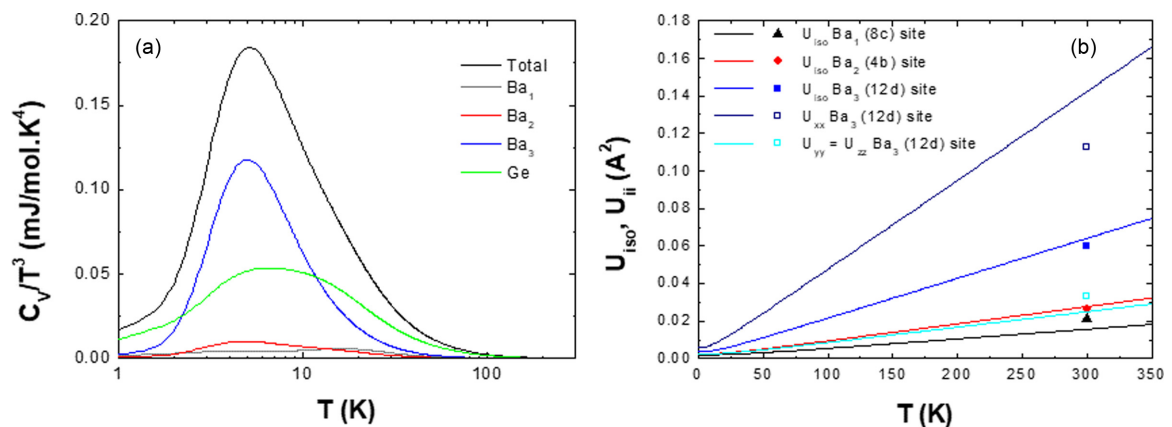


FIG. 6. (a) Debye plot of the total and partial heat capacity as a function of temperature. (b) Atomic displacement parameters of barium atoms in  $\text{Ba}_{24}\text{Ge}_{100}$  from density functional theory (DFT) calculations compared with experimental results of Fukuoka *et al.* [11].

TABLE II. Characteristic energies and potential parameters of Ba guests in  $\text{Ba}_{24}\text{Ge}_{100}$  derived from DFT results.  $K_2$ ,  $K_3$ , and  $K_4$  are the harmonic and anharmonic parameters from fitting the potentials with the polynomial function  $y = K_2\Delta x^2 + K_3\Delta x^3 + K_4\Delta x^4$ .  $E_2$  corresponds to the characteristic energies calculated from  $K_2$ , and the dimensionless anharmonic parameter  $\beta$  is computed from the quartic force constant  $K_4$  according to the Dahm-Ueda model [58].

Guest atom	$K_2(\text{eV}/\text{\AA}^2)$	$K_3(\text{eV}/\text{\AA}^3)$	$K_4(\text{eV}/\text{\AA}^4)$	$E_2$ (meV)	$\beta$
Ba1 (8c)	1.37	0.23	0.75	6.5	0.010
Ba2 (4b)	1.14		0.87	5.9	0.016
Ba3 [100] (12d)	0.2	0.00	0.09	2.5	0.023
Ba3 [001] (12d)	1.04	-0.26	0.89	5.6	0.018

our high-resolution INS experiments, we observe its intensity to be strongest at distinguished  $Q$  points of highest Bragg peak intensity and density, i.e., at 2.3 and 3.5  $\text{\AA}^{-1}$ .

To shed more light on the underlying modes forming the 2.2 meV peak in the DFT data, we have computed the Ba atomic potentials as a function of the displacements  $\Delta x$  along nonequivalent, high-symmetry directions. The results are plotted in Fig. 5(a). A polynomial function  $\Delta E(\Delta x) = K_2\Delta x^2 + K_3\Delta x^3 + K_4\Delta x^4$  was fitted to the data to quantify the force constants and the degree of anharmonicity of the Ba vibrations. The harmonic  $K_2$  and anharmonic cubic  $K_3$  and quartic  $K_4$  terms are reported in Table II. The anharmonicity of the atomic potentials will be discussed latter.

Any sampled potential energy takes on a minimum at  $\Delta x = 0$ ; thus, the equilibrium positions of any Ba are at the center of the cages. The harmonic force constants of Ba1, Ba2, and Ba3 along [010]/[001] are rather similar. The decreasing values of  $K_2$  in the sequence of Ba1, Ba2, and Ba3 potentials underline the behavior of the corresponding partial DOS to be located at progressively lower energies shown in Fig. 1. The striking result is the strong depletion of the Ba3 potential along [100]. The associated force constant is smaller than a factor of 5 in comparison with the other values. Consequently, the low-energy peak at 2.2 meV is dominated by the vibrations of Ba3 atoms on (12d) sites with elongations along the largest dimension of the Ge@20 cages, i.e., [100]. We corroborate this statement by presenting the directional partial DOS of the Ba3 atoms in Fig. 5(b).

Similar results have been obtained for Ba3 atoms in  $\text{Ba}_{24}\text{Si}_{100}$  [12]. However, in the germanide case, the harmonic  $K_2$  of Ba1 and Ba3 along the high-symmetry directions are almost two times smaller than in the silicide counterpart. This signifies softer bonding and smaller guest vibrational energies in  $\text{Ba}_{24}\text{Ge}_{100}$ , as pointed out above. When compared with  $\text{Ba}_8\text{Ge}_{43}$ , we find here smaller  $K_2$  of the guest atoms of up to a factor of 2 for Ba3 along the high-symmetry direction [34]. This explains the guest lowest energy among the studied Si- and Ge-based clathrates.

The presence of low-energy Ba-weighted modes are perceivable in other phonon-related observables such as specific heat and ADPs. In Fig. 6(a), we report the Debye plot of the heat capacity ( $C_v/T^3$  vs  $T$ ) of  $\text{Ba}_{24}\text{Ge}_{100}$  obtained from the DFT calculations. We observe a maximum at  $\sim 5$  K caused by the deviation from the Debye model due to the modes at 2–3 meV. This corroborates the observation done for  $\text{Ba}_{24}\text{Si}_{100}$ , where a peak at the higher temperature of 8 K [12] is associated with a larger and anisotropic Debye-Waller factor

of the Ba3 atoms, a fingerprint of low-energy optical modes. The notable contribution from the Ge atoms corroborates once more the noteworthy coupling between the Ba guests and the host network. Note that the computation of the  $C_v/T^3$  properties with the high-temperature structure makes a comparison with experimental data as reported by Paschen *et al.* [17] impractical.

In Fig. 6(b), we compare the anisotropic  $U_{ii}$  and isotropic ADPs  $U_{iso}$  of the Ba atoms in  $\text{Ba}_{24}\text{Ge}_{100}$  with experimental data. The computed values at 300 K are as well indicated in

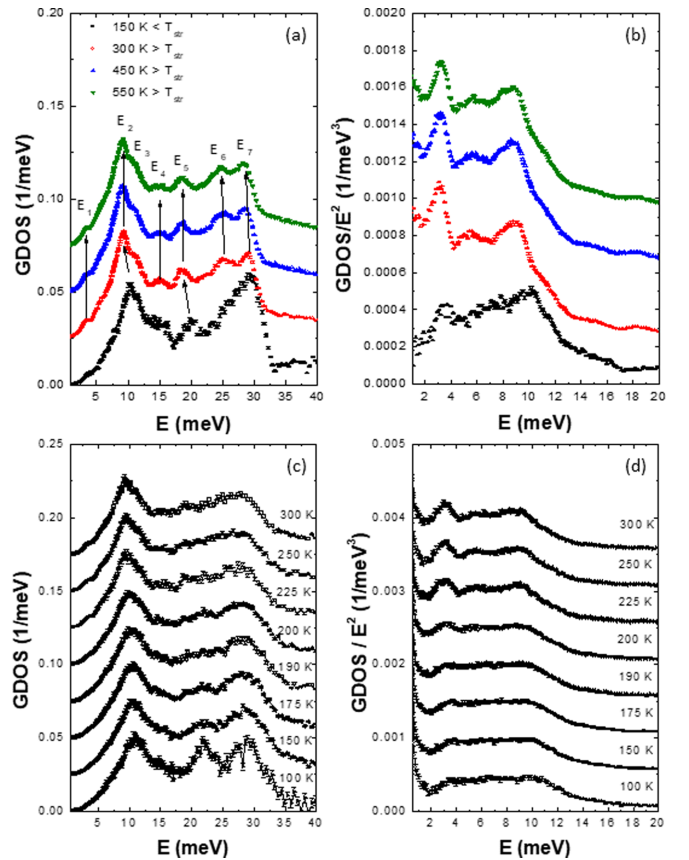


FIG. 7. (a) Generalized density of states (GDOS) of  $\text{Ba}_{24}\text{Ge}_{100}$  as a function of temperature derived from inelastic neutron scattering (INS) experiments at IN5 with the incident wavelength of 5  $\text{\AA}$ . (b) Same datasets in a Debye plot  $\text{GDOS}/E^2$  vs  $E$ . (c) GDOS from INS measurements at IN6 with an incident wavelength of 4.14  $\text{\AA}$ . (d) Same datasets in a Debye plot  $\text{GDOS}/E^2$  vs  $E$ .



TABLE III. Anisotropic ADPs of Ba<sub>24</sub>Ge<sub>100</sub> at 300 K from DFT calculations.

Atoms	Wyckoff	U <sub>11</sub> (Å <sup>2</sup> )	U <sub>22</sub> (Å <sup>2</sup> )	U <sub>33</sub> (Å <sup>2</sup> )	U <sub>12</sub> (Å <sup>2</sup> )	U <sub>13</sub> (Å <sup>2</sup> )	U <sub>23</sub> (Å <sup>2</sup> )
Ba1	8c	0.0157	U <sub>11</sub>	U <sub>11</sub>	0.0006	U <sub>12</sub>	U <sub>12</sub>
Ba2	4b	0.0277	U <sub>11</sub>	U <sub>11</sub>	0.0084	U <sub>12</sub>	U <sub>12</sub>
Ba3	12d	0.1424	0.025	U <sub>22</sub>	0.0065	-0.0066	0.0061
Ge1	8c	0.0264	U <sub>11</sub>	U <sub>11</sub>	0.0039	U <sub>12</sub>	U <sub>12</sub>
Ge2	24e	0.0182	0.0162	0.0152	0.0012	0.0028	-0.0022
Ge3	12d	0.0208	0.0159	U <sub>22</sub>	-0.0021	0.0021	0.0046
Ge4	24e	0.0189	0.0178	0.0157	0.0002	0.001	-0.0047
Ge5	24e	0.0274	0.0167	0.0145	-0.0032	0.0005	0.0013
Ge6	8c	0.0173	U <sub>11</sub>	U <sub>11</sub>	-0.0034	U <sub>12</sub>	U <sub>12</sub>

Tables I and III. The isotropic ADPs  $U_{\text{iso}}$  of the Ge atoms are reported in Appendix B. Because of the site symmetry, the ADPs of Ba1 and Ba2 atoms are isotropic, and we only report their  $U_{\text{iso}}$ . The largest values of the  $U_{ii}$  of the Ba3 atoms are along the high-symmetry direction and for the largest dimension of the open Ge@20 cage, here for  $U_{xx}$ . As outlined above, it is the consequence of the low-energy Ba3 modes in this direction. The comparison with experimental results by Fukuoka *et al.* [13] reveals a rather good agreement. This is also the case for other experiments reporting ADPs [14,15,53]. Similarly, anisotropic and large  $U_{ii}$  have been reported for other type-IX clathrates, and notably large ADPs of guest atoms in the high-symmetry direction of the M@20 open cages ( $M = \text{Si, Ge, Sn}$ ) have been observed for all compounds with type-IX clathrate structure due to the asymmetric shape of these cages [13–15,28–30,54–56].

The examination of the atom projected DOS (Fig. 1) suggests a much stronger correlation of Ba with Ge atoms in Ba<sub>24</sub>Ge<sub>100</sub> than of Ba with Si in Ba<sub>24</sub>Si<sub>100</sub> [12]. This can be seen in the notable contribution of the lighter Ge atoms to the lowest energy modes at 2–3 meV as well as the participation of the heavy Ba atoms to higher energy vibrations. In Ba<sub>24</sub>Si<sub>100</sub>, those effects are less prominent. We highlight the significant contribution as well of Ba1 atoms to the peak at ~7–8 meV as well as the participation of Ba3 to the peak ~13 meV dominated by Ge3 and Ge5 atoms. Above 16 meV, the signal from Ba is rather depleted in the phonon DOS, and the dynamics is ruled by Ge atoms with alternating contributions from the different sites.

We discuss next the effect of temperature and the temperature-induced structure transformation on the vibrational dynamics. Temperature-dependent GDOS data derived from INS experiments at different conditions with the spectrometers IN5 and IN6 are presented in Figs. 7 and 8(a). Energies of characteristic peaks found in the GDOS data are listed in Table IV. When crossing the region of the structural

transition toward low  $T$ , one can clearly see (i) a depletion of intensity of the peak at ~3.3 meV [Figs. 7(b) and 7(d)], (ii) a strong upshift of the peak at ~10 meV [Figs. 7(a), 7(c), and 8(a)], (iii) a concomitant disappearance of the shoulder at ~11–12 meV, and (iv) a strong upshift of the peak at ~19 meV [Fig. 7(a)]. Compared with these strong spectral modifications, the GDOS changes very little above the temperature region of structure transformation (190–230 K). As expected from a moderately anharmonic compound, an overall weak softening of phonons up to 550 K is observed. The low-energy peak dominated by the Ba3 dynamics, however, appears rather insensitive to this temperature-induced volume expansion. This indicates a smaller anharmonicity of Ba3 in Ba<sub>24</sub>Ge<sub>100</sub> than in Ba<sub>24</sub>Si<sub>100</sub> [12]. Note that the opposite behavior is observed in type-I clathrates, where Ba<sub>8</sub>Si<sub>46</sub> is found less anharmonic than the ternary type-I Ba-Ga-Ge and Ba-Zn-Ge [8,35,52] compounds. Similar weak anharmonicity of the low-energy optic modes was observed in Ba<sub>8</sub>Ge<sub>43</sub> [35].

On the contrary, strong spectral modifications of the GDOS occur in the low-energy range of Ba-dominated vibrations between 230 K and 190 K, i.e., when cooling through the phase transformation region. Equally, a progressive tapering of the dominating peaks ~22 and 30 meV indicates a spectral modification of the Ge-dominated excitations.

A rather intriguing behavior is detected for the vibrational modes forming the peak at ~3.3 meV in the GDOS, as it is documented in Fig. 4. Above the structural transition, a localized mode band visible at any  $Q$  point of the powder spectra is observed. The powder-averaged form factor indicates that the intensity is, however, particularly strong at points of strong signals from acoustic phonons.

To elaborate on this observation, we present cuts through the inelastic response at constant energy and wave vector transfers in Figs. 9 and 10 as well as in Fig. 16 in Appendix C. The plotted signal is the temperature-corrected susceptibility divided by the energy transfer for better visibility of

TABLE IV. Temperature variation of peak energies of Ba<sub>24</sub>Ge<sub>100</sub> obtained from GDOS data derived from an IN5 experiment with 5 Å incident neutron wavelength. Corresponding peaks are indicated in Fig. 7(a).

$T$ (K)	$E_1$ (meV)	$E_2$ (meV)	$E_3$ (meV)	$E_4$ (meV)	$E_5$ (meV)	$E_6$ (meV)	$E_7$ (meV)
150	3.8	10.4			20.1		29.5
300	3.3	9.4	10.8	15.2	18.9	25.2	29.3
450	3.3	9.2	10.8	15.2	18.8	25.5	28.8
550	3.3	9.2	10.5	15	18.77	24.8	28.6

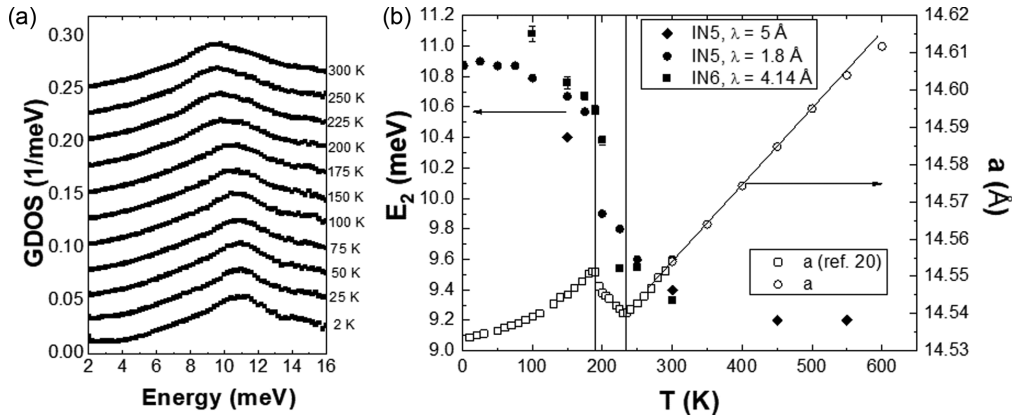


FIG. 8. (a) GDOS of  $\text{Ba}_{24}\text{Ge}_{100}$  as function of temperature derived from IN5 data recorded with the incident wavelength of  $1.8 \text{ \AA}$ . (b) Variation of the strong peak at  $10 \text{ meV}$  as a function of temperature identified in all our inelastic neutron scattering (INS) experiments as well as temperature dependence of the lattice parameter of  $\text{Ba}_{24}\text{Ge}_{100}$  at low (Ref. [20]) and high temperature (our data) upon heating.

the low-energy signal. From the carried-out cuts, it is obvious to conclude that Brillouin zone center excitations contribute to this vibrational band with prominent eigenvectors, as the intensity is most prominent in  $Q$  regimes of acoustic phonons emanating from strong Bragg reflections, i.e., Brillouin zone centers.

This conclusion holds as well for temperatures below the structural transition. However, the peak intensity is diminished in comparison with the signal from acoustic phonons. It appears thus more concentrated around  $Q$  points of high Bragg peak intensity and density in the powder signal.

As evidenced in Fig. 10(a), the low-energy peak is just detectable at the  $Q$  points of acoustic signal; it is narrower than above the phase transition [Fig. 10(b)], and most importantly, it seems to be shifted to higher energies by  $\sim 0.5 \text{ meV}$ . Appendix C [Fig. 16] highlights this behavior for higher  $Q$  points with lower energy resolution.

To demonstrate the correlation of the changes in the inelastic response of  $\text{Ba}_{24}\text{Ge}_{100}$  with the structural transition, we compile in Fig. 8(b) the location of the dominating peak  $\sim 10 \text{ meV}$  from all our  $T$ -dependent INS measurements. For comparison, we report the lattice parameter measured by Carrillo-Cabrera *et al.* [20] from base to room tempera-

ture, i.e., crossing the phase transition, and our experimental data expanding the  $T$  range up to  $600 \text{ K}$ . Clearly, in any of the INS datasets, the changes in the peak position occur when the temperature-induced structure transformation takes place. Note that the peak downshifts within only  $40 \text{ K}$  by  $\sim 10\%$  upon heating. In the two temperature domains of structural stability, namely,  $<190 \text{ K}$  and  $>230 \text{ K}$ , the peak energy changes only moderately by  $\sim 2\%$  within several hundred Kelvin. As the behavior in the high  $T$  modification is concerned, the low anharmonicity is in line with our DFT data discussed above. We recall that the computed potentials shown in Fig. 5(a) exclude off-centering of any of the Ba positions in the high-temperature phase.

As shown in Fig. 1, the vibrations in this energy range are strongly reminiscent of the dynamics of Ba1, Ba2, and Ge. Thus, with the temperature response of the low-energy peak being dominated by the Ba3 dynamics, we conclude that the structural variation taking place in the temperature range  $190\text{--}230 \text{ K}$  takes strong influence on the inelastic response of all three Ba sites concomitantly. The enhancement of their characteristic frequencies gives evidence of a stronger bonding and higher correlation with the dynamics of Ge below the transition.

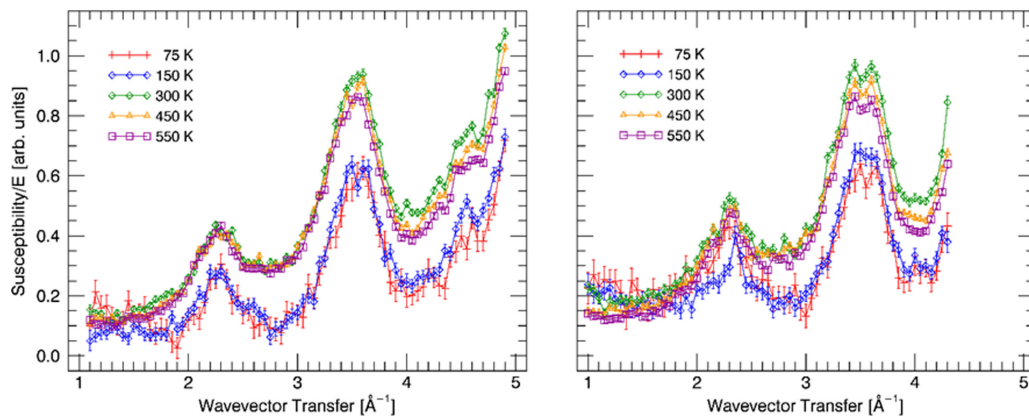


FIG. 9. Constant energy cuts through the dynamic susceptibility divided by the energy for  $3.5 \pm 0.5 \text{ meV}$  from IN5 experiments with  $\lambda = 2.5 \text{ \AA}$ . (left) Anti-Stokes line, and (right) Stokes line.  $20 \text{ K}$  data not shown due to enhanced background contribution. Wave vector transfers with peaking signal ( $2.3$  and  $3.5 \text{ \AA}^{-1}$ ) correspond to points with strong Bragg peak intensities and densities the origin of acoustic phonon signal. Note the overall sudden reduction of signal below the temperature of structural transition.



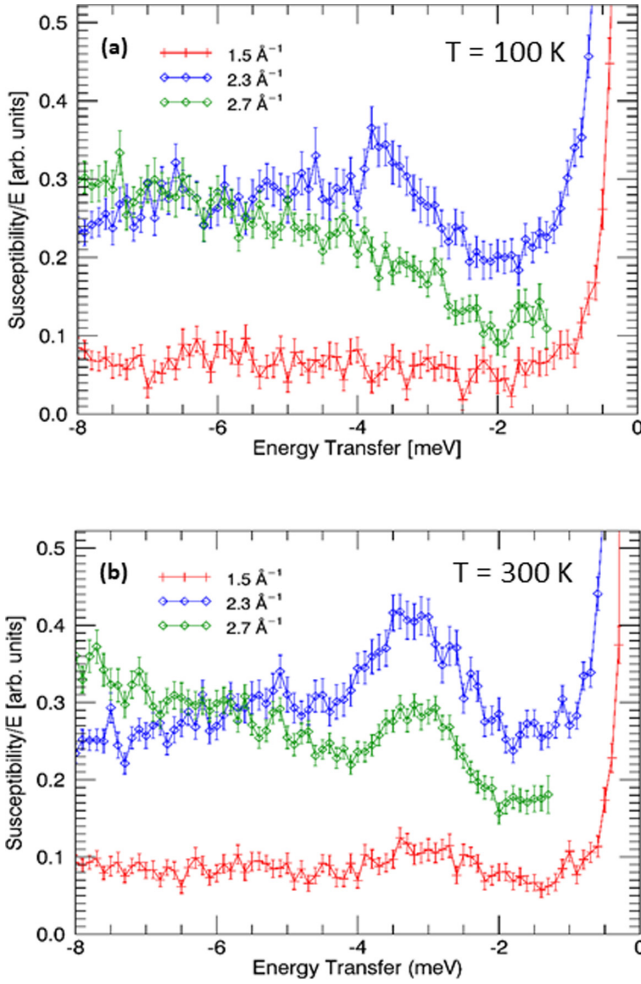


FIG. 10. Constant wave vector cuts through the dynamic susceptibility divided by the energy from IN6 experiments with  $\lambda = 4.14 \text{ \AA}$  at (a) 100 K and (b) 300 K. Only anti-Stokes line intensity is shown. Note that, at 300 K, the well-defined low-energy peak  $\sim 3 \text{ meV}$  persists at  $Q$  points away from high Bragg peak intensity  $\sim 2.3 \text{ \AA}^{-1}$ . This feature is not detectable in the inelastic response below the structural phase transition at 100 K.

To quantify the anharmonicity of the DFT calculated structure, i.e., the high  $T$  phase, and set it in relation to literature data, we use the simple model of the anharmonic, isolated oscillator derived by Dahm and Ueda [57]. In this approach, the renormalization of the eigenenergy of a harmonic oscillator  $E_0(T)$ , derived as

$$\left[ \frac{E_0(T)}{E_0(T=0)} \right]^2 = 1 + \beta \frac{E_0(T)}{E_0(T=0)} \left\{ \frac{1}{\exp\left[\frac{E_0(T)}{k_B T}\right]} - 1 \right. \\ \left. + \frac{1}{2} - \frac{1}{2} \frac{E_0(T)}{E_0(T=0)} \right\},$$

is given by the anharmonic quartic term  $K_4$  whose amplitude is expressed by the dimensionless parameter  $\beta = 4K_4\hbar^4/E_0(T=0)^3M^2$  [57]. Both  $K_4$  and  $\beta$  of the different Ba atoms of  $\text{Ba}_{24}\text{Ge}_{100}$  are calculated from the fit of the atomic potential with a polynomial function in Fig. 5(a) and listed in

Table II. These values are moderate but not negligible, especially for the vibrations of Ba3 along [100]. They are slightly larger in  $\text{Ba}_{24}\text{Ge}_{100}$  than in  $\text{Ba}_{24}\text{Si}_{100}$ , which is a surprising result at first glance, as we have observed a softening of the lowest energy optical modes in  $\text{Ba}_{24}\text{Si}_{100}$  upon cooling [12], which is missing in  $\text{Ba}_{24}\text{Ge}_{100}$ .

There are two contributions in the thermal variation of the phonon energies  $dE/dT$  [58,59]. On one hand, there is the implicit quasiharmonic contribution due to the volume change  $dE_{\text{impl}}/dT = -\alpha_V \gamma E(T \rightarrow 0 \text{ K})$  with  $\alpha_V$  being the volume thermal expansion and  $\gamma$  the mode Grüneisen parameter and, on the other, the explicit anharmonic contribution due to the thermal population of the vibrational levels  $dE_{\text{expl}}/dT$ . If  $\alpha_V$  and  $\gamma$  are positive,  $dE_{\text{impl}}/dT$  would be negative and could compensate the positive  $dE_{\text{expl}}/dT$ , when  $\beta$  is positive, to explain the absence of temperature dependence of the lowest energy optical modes in  $\text{Ba}_{24}\text{Ge}_{100}$ . With these conditions, we conjecture that  $\alpha_V \gamma$  should be larger in  $\text{Ba}_{24}\text{Ge}_{100}$  than in  $\text{Ba}_{24}\text{Si}_{100}$  because  $\beta$  is larger and hence  $dE_{\text{expl}}/dT$  in  $\text{Ba}_{24}\text{Ge}_{100}$  than in  $\text{Ba}_{24}\text{Si}_{100}$  [12].

From linear fitting of the lattice parameter between 300 and 500 K [see Fig. 8(b) for data], we determine the linear thermal expansion  $\alpha = \alpha_V/3 = 14.13 \text{ MK}^{-1}$  of  $\text{Ba}_{24}\text{Ge}_{100}$ . This value is slightly larger than for  $\text{Ba}_8\text{Ge}_{43}$  ( $\alpha = 12.65 \text{ MK}^{-1}$ ),  $\text{Ba}_8\text{Zn}_x\text{Ge}_{46-x}$  ( $\alpha = 11.3$  to  $13 \text{ MK}^{-1}$ ) and larger or similar than for  $\text{Ba}_8\text{Ga}_{16}\text{Ge}$  ( $\alpha = 10$  to  $14.2 \text{ MK}^{-1}$ ) [60] as well as larger than for  $\text{Ba}_{24}\text{Si}_{100}$  ( $\alpha = 10.6 \text{ MK}^{-1}$ ) and  $\text{Ba}_8\text{Si}_{46}$  ( $\alpha = 12.25 \text{ MK}^{-1}$ ) [8]. For the silicides, the thermal expansion is smaller in the type-I than in the type-IX clathrates in contrast to the germanide clathrates.

From data of pressure-dependent Raman spectroscopy on  $\text{Ba}_{24}\text{Ge}_{100}$  [31] and measured bulk modulus ( $B = 44 \text{ GPa}$ ) [27], we determine the rather low Grüneisen parameter  $\gamma = 0.9$  for the Raman line at  $31.5 \text{ cm}^{-1}$  ( $4 \text{ meV}$ ). Further, we calculate  $dE_{\text{impl}}/dT = -0.0012 \text{ cm}^{-1}/\text{K}$  (i.e.,  $-0.15 \mu\text{eV}/\text{K}$ ), which results in a decrease of the energy by  $\sim 0.04 \text{ meV}$  between 300 and 550 K. This value is too small to be seen in the INS experiments. Note that it is as well about one order of magnitude smaller than the energy variation expected from the explicit contribution determined from the DFT calculations. This means that  $dE_{\text{expl}}/dT$  and hence  $\beta$  of  $\text{Ba}_{24}\text{Ge}_{100}$  are greatly overestimated by our DFT calculations. This contrasts with the case of  $\text{Ba}_{24}\text{Si}_{100}$  for which  $\beta$  obtained from the DFT calculations was in reasonable agreement with that obtained from the experiments [12].

With the knowledge of the volume thermal expansion  $\alpha_V$ , the molar volume  $V_m$ , the molar heat capacity  $C_P$  [17], and the bulk modulus  $B$  [27] of  $\text{Ba}_{24}\text{Ge}_{100}$  at 300 K, we compute the thermodynamic Grüneisen parameter  $\Gamma = \alpha_V B V_m / C_P$  to 1.12. This is a lower value than those of  $\text{Ba}_{24}\text{Si}_{100}$  ( $\Gamma = 1.78$ ) and  $\text{Ba}_8\text{Si}_{46}$  ( $\Gamma = 1.88$ ) that have been calculated from the data of Lortz *et al.* [8], Toulemonde *et al.* [61], and San Miguel *et al.* [62]. This difference is mainly due to the smaller bulk modulus of  $\text{Ba}_{24}\text{Ge}_{100}$  than for Ba-Si clathrates.

#### IV. CONCLUSIONS

We have reported a combined experimental and theoretical study of the LD of the type-IX clathrate  $\text{Ba}_{24}\text{Ge}_{100}$ . There

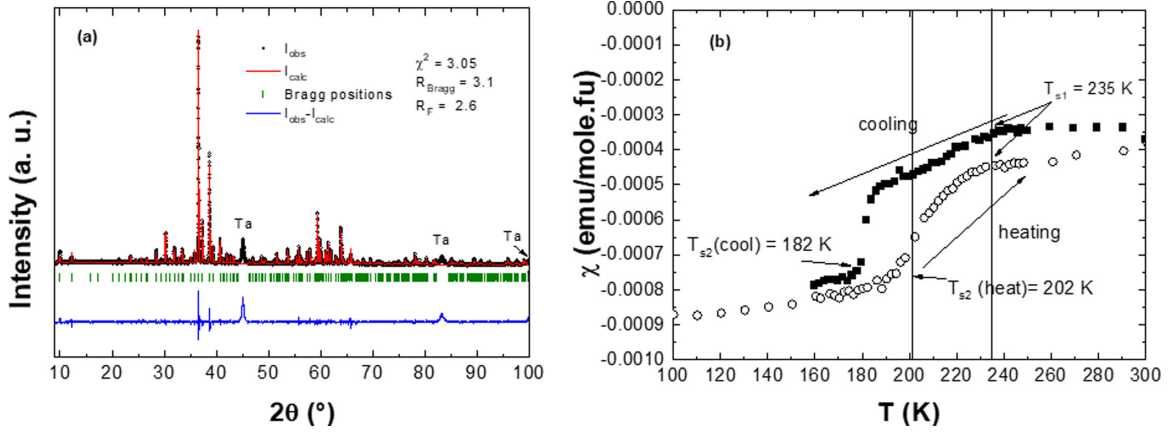


FIG. 11. (a) LeBail refinement of the x-ray diffraction (XRD) pattern of  $\text{Ba}_{24}\text{Ge}_{100}$  at 300 K. (b) Thermal variation of the magnetic susceptibility of  $\text{Ba}_{24}\text{Ge}_{100}$ .

is good qualitative agreement between the GDOS obtained by the INS experiments and the DOS obtained by the DFT calculations. The experimental ADPs from the literature are well reproduced qualitatively by the DFT calculations. The origin of the low-energy Raman-active modes are obtained thanks to the DFT calculations. The peak at  $\sim 3$  meV in the GDOS from the INS experiment is due to the low-energy optical modes stemming from the motions of the  $\text{Ba}_3$  guest atom along the high-symmetry direction and the largest dimensions of the open  $\text{Ge}_{20}$  cages. We find that the characteristic energy of the peak has no temperature dependence in the high-temperature phase, and its intensity is strongly depleted as well as apparently shifted to higher energies across the phase transition at low temperature. The absence of temperature dependence of the peak at 3.3 meV in the high-temperature phase could be due to a compensation of a softening effect due to the fourth-order anharmonicity by the volume contraction upon cooling. We also observed a large change in the spectral weight when the phase transition takes place and

especially a large shift of the peak at  $\sim 10$  meV. We find that  $\text{Ba}_{24}\text{Ge}_{100}$  has a moderate thermodynamic Grüneisen parameter being significantly smaller than those of  $\text{Ba}_{24}\text{Si}_{100}$  and  $\text{Ba}_8\text{Si}_{46}$ .

#### ACKNOWLEDGMENTS

We acknowledge the support of the project with the beam time CRG-2534 (Phenix-#623, DOI:10.5291/ILL-DATA.CRG-2534) on the instrument IN6-Sharp as well as by the IN6-Sharp team. We are equally grateful for the ILL beam time (DOI: 10.5291/ILL-DATA.TEST-2919) on the instrument IN5.

#### APPENDIX A: SAMPLE CHARACTERIZATION

The polycrystalline sample is single phase, as shown by the refinement with the LeBail method of the XRD data at 300 K with very good refinement quality factors in the Fig. 11(a).

TABLE V. Calculated Raman-active modes at  $\Gamma$  point for  $\text{Ba}_{24}\text{Ge}_{100}$  from DFT.

Raman modes	Calculated frequency modes (in $\text{cm}^{-1}$ )
$A_1$ symmetry	24.9; 56.3; 61.4; 72.1; 90.8; 93.6; 132; 139.9; 169.6; 183.4; 190.1; 202.1; 217.4; 222.6
$E$ symmetry	18.8; 27.2; 35.8; 42.7; 50.4; 54.2; 55.8; 60.1; 61.3; 63.7; 67.3; 74.1; 79.5; 80.9; 88.9; 107.8; 112.9; 135.5; 141.1; 157.8; 160.9; 168.3; 181.1; 185.6; 188.3; 193.6; 194; 202.2; 213.7; 217.8; 220.9
$T_2$ symmetry	20.1; 32.9; 37.2; 40.6; 43.2; 46.7; 52; 56.8; 59.3; 62; 62.9; 65.6; 66.4; 67.5; 70.2; 75.1; 76.4; 78.9; 83.1; 90.6; 105.8; 112; 120.9; 133.4; 134.7; 139.4; 146.7; 153.8; 160.3; 163.7; 169.6; 175.4; 177.9; 188; 188.4; 190.9; 194.3; 196.4; 202.9; 204.2; 210.8; 215.1; 216.6; 221.9; 223.3
Calculated infrared-active modes at $\Gamma$ point for $\text{Ba}_{24}\text{Ge}_{100}$ from DFT.	
Infrared modes	Calculated frequency modes (in $\text{cm}^{-1}$ )
$T_1$ symmetry	16.5; 18.3; 29.7; 37.7; 42.3; 46; 53.2; 53.8; 57.6; 58.4; 59.5; 60.4; 63; 64.3; 67.1; 69.5; 70.5; 74.2; 76.8; 81.3; 83.9; 88.4; 92.2; 104.9; 108.5; 113.8; 129.2; 130.8; 141.2; 144; 155.3; 158.8; 166.2; 172.7; 176.8; 185.4; 188.2; 189.5; 191.5; 195.4; 197.6; 204.5; 212.6; 214; 215.4; 221.8; 222.7
Calculated optically silent modes at $\Gamma$ point for $\text{Ba}_{24}\text{Ge}_{100}$ from DFT.	
Silent modes	Calculated frequency modes (in $\text{cm}^{-1}$ )
$A_2$ symmetry	19.9; 21.8; 43.4; 53.9; 63.3; 64.6; 71.6; 80.4; 96.6; 119.5; 140.1; 146; 154.2; 169.3; 201.4; 209.5; 223

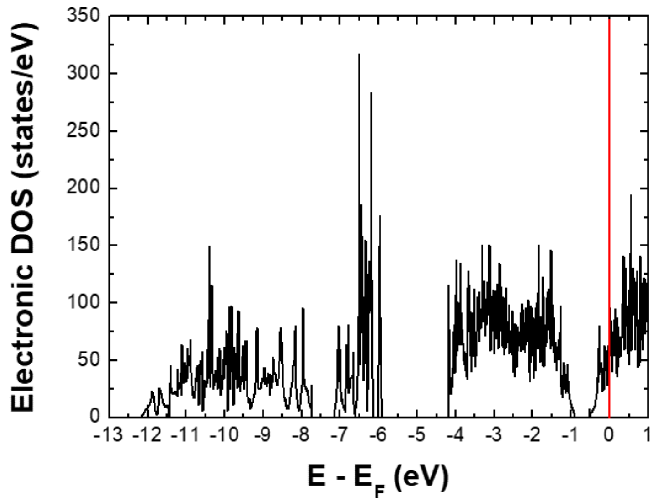


FIG. 12. Electronic density of states of  $\text{Ba}_{24}\text{Ge}_{100}$  from density functional theory (DFT) calculations.

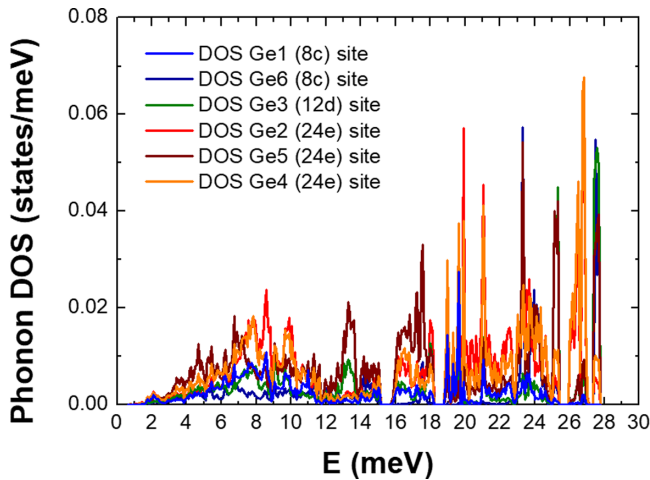


FIG. 13. Atom-projected phonon density of states of the Ge atoms of  $\text{Ba}_{24}\text{Ge}_{100}$  obtained from density functional theory (DFT) calculations.

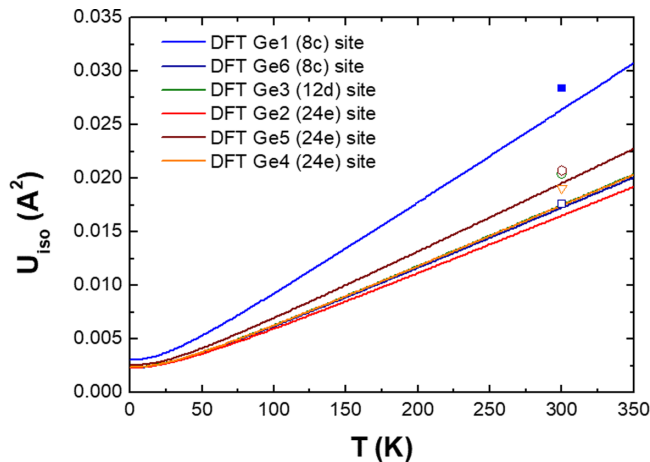


FIG. 14. Isotropic atomic displacements parameters  $U_{\text{iso}}$  of germanium atoms of  $\text{Ba}_{24}\text{Ge}_{100}$  from density functional theory (DFT) calculations compared to experimental results of Fukuoka *et al.* [13].

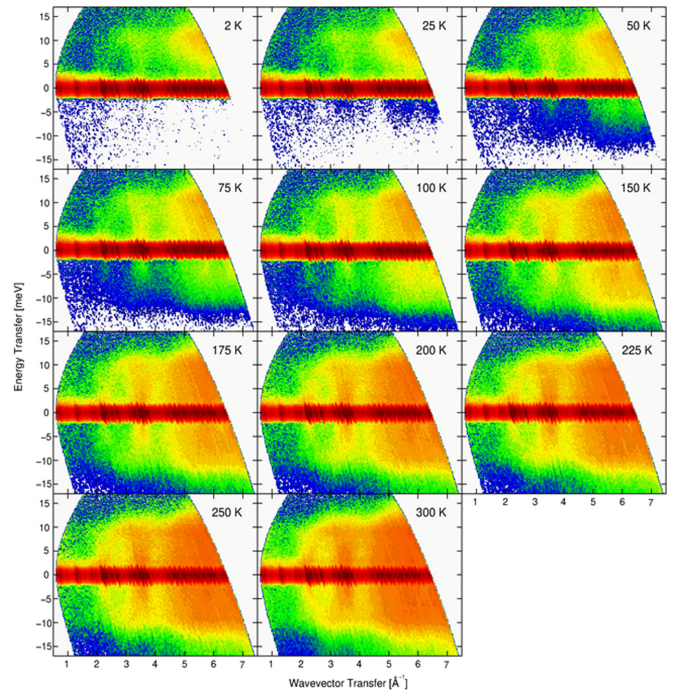


FIG. 15. Intensity maps of the dynamic structure factor of  $\text{Ba}_{24}\text{Ge}_{100}$  measured on IN5 with an incident wavelength of  $1.8 \text{ \AA}$  at the indicated temperatures. Positive energies denote the Stokes line, negative energies the anti-Stokes line signals.

The XRD patterns have been measured at high temperatures with a  $\text{Co K}\alpha$  source. The peaks at  $\sim 45^\circ$ ,  $83^\circ$ , and  $100^\circ$  are due to the Ta heating plate and are not considered in the LeBail refinement. The lattice parameters at high temperature have been obtained by refinement using the LeBail method.

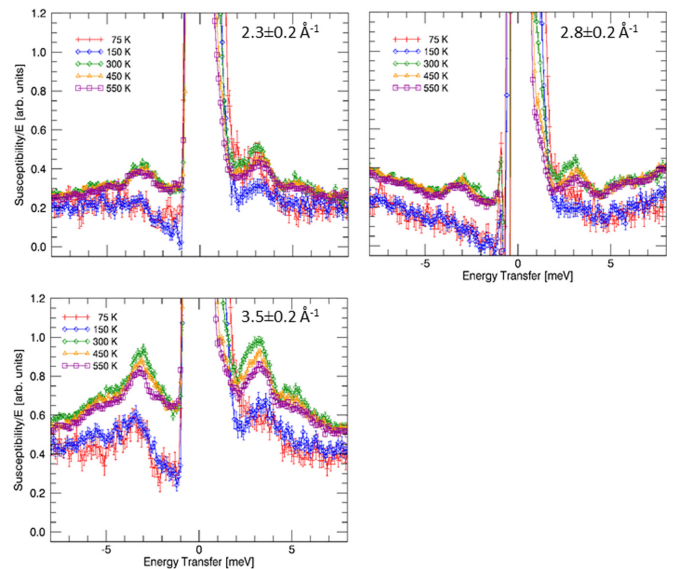


FIG. 16.  $Q$  cut through the dynamic susceptibility divided by the energy for  $2.3 \pm 0.2$ ,  $2.8 \pm 0.2$ , and  $3.5 \pm 0.2 \text{ \AA}^{-1}$ , from IN5 experiments with  $\lambda = 2.5 \text{ \AA}$ . (left) Anti-Stokes line, and (right) Stokes line. 20 K data not shown due to enhanced background.



To follow the structural transition and determine the transition temperatures  $T_{s1}$  and  $T_{s2}$  in our sample, we report the magnetic susceptibility with cooling and heating profiles in Fig. 11(b), as it has been done by Grosche *et al.* [16] and Paschen *et al.* [17]. Our results agree well with these works [16,17].

## APPENDIX B: COMPLEMENTARY DFT RESULTS

We present here additional useful results from DFT calculations.

The electronic DOS in Fig. 12 is in very good agreement with the calculations of Zerec *et al.* [21]. We report in Table V the frequencies and the symmetries of the different optical modes of  $\text{Ba}_{24}\text{Ge}_{100}$  at the  $\Gamma$  point from DFT calculations. We report in Fig. 13 in the atom-projected DOS

of the different Ge atoms in  $\text{Ba}_{24}\text{Ge}_{100}$  from DFT calculations. We report in Fig. 14 the isotropic ADPs  $U_{\text{iso}}$  of the different Ge atoms in  $\text{Ba}_{24}\text{Ge}_{100}$  from DFT calculations and compare them with experimental results from Fukuoka *et al.* [13].

## APPENDIX C: LOW-RESOLUTION INS RESULTS

We report the density maps recorded at IN5 with 1.8 Å incident wavelength and different temperatures in Fig. 15. We report in Fig. 16 the  $Q$  cut through the dynamic susceptibility divided by the energy for  $2.3 \pm 0.2$ ,  $2.8 \pm 0.2$ , and  $3.5 \pm 0.2 \text{ \AA}^{-1}$  from IN5 experiments with  $\lambda = 2.5 \text{ \AA}$ . The data highlight the consistent behavior of the previously discussed low-energy excitations at higher  $Q$  numbers. Note that, at the lowest  $T$  of 75 K, the susceptibility at the Stokes line is obscured by the strong elastic intensity  $<4 \text{ meV}$ .

- 
- [1] G. J. Snyder and E. S. Toberer, *Nat. Mat.* **7**, 105 (2008) and refs. therein.
- [2] G. A. Slack, in *CRC Handbook of Thermoelectricity*, edited by D. M. Rowe (CRC Press, Boca Raton, 1995), Chap. 34, p. 407.
- [3] B. C. Sales, D. Mandrus, and R. K. Williams, *Science* **272**, 1325 (1996).
- [4] M. Christensen, S. Johnsen, and B. B. Iversen, *Dalton Trans.* **39**, 978 (2010).
- [5] C. H. Lee, I. Hase, H. Sugawara, H. Yoshizawa, and H. Sato, *J. Phys. Soc. Jpn.* **75**, 123602 (2006).
- [6] M. M. Koza, M. R. Johnson, R. Viennois, H. Mutka, L. Girard, and D. Ravot, *Nat. Mater.* **7**, 805 (2008).
- [7] M. M. Koza, M. Boehm, E. Sischka, W. Schnelle, H. Mutka, and A. Leithe-Jasper, *Phys. Rev. B* **91**, 014305 (2015).
- [8] R. Lortz, R. Viennois, A. Petrovic, Y. Wang, P. Toulemonde, C. Meingast, M. M. Koza, H. Mutka, A. Bossak, and A. San Miguel, *Phys. Rev. B* **77**, 224507 (2008).
- [9] H. Mutka, M. M. Koza, M. R. Johnson, Z. Hiroi, J.-I. Yamaura, and Y. Nagao, *Phys. Rev. B* **78**, 104307 (2008).
- [10] M. M. Koza, H. Mutka, Y. Okamoto, J.-I. Yamaura, and Z. Hiroi, *Phys. Chem. Chem. Phys.* **17**, 24837 (2015).
- [11] T. Takabatake, K. Suekuni, T. Nakayama, and E. Kaneshita, *Rev. Mod. Phys.* **86**, 669(2014).
- [12] R. Viennois, M. M. Koza, R. Debord, P. Toulemonde, H. Mutka, and S. Pailhès, *Phys. Rev. B* **101**, 224302 (2020).
- [13] H. Fukuoka, K. Iwai, S. Yamanaka, H. Abe, K. Yoza, and L. Häming, *J. Solid State Chem.* **151**, 117 (2000).
- [14] S.-J. Kim, S. Hu, C. Uher, T. Hogan, B. Huang, J. D. Corbett, and M. G. Kanatzidis, *J. Solid State Chem.* **153**, 321 (2000).
- [15] W. Carrillo-Cabrera, J. Curda, H. G. von Schnering, S. Paschen, and Y. Grin, *Z. Kristallogr.* **215**, 207 (2000).
- [16] F. M. Grosche, H. Q. Yuan, W. Carrillo-Cabrera, S. Paschen, C. Langhammer, F. Kromer, G. Sparn, M. Baenitz, Y. Grin, and F. Steglich, *Phys. Rev. Lett.* **87**, 247003 (2001).
- [17] S. Paschen, V. H. Tran, M. Baenitz, W. Carrillo-Cabrera, Y. Grin, and F. Steglich, *Phys. Rev. B* **65**, 134435 (2002).
- [18] V. Petkov and T. Vogt, *Solid State Commun.* **127**, 43 (2003).
- [19] M. Schmidt, P. G. Radaelli, M. J. Gutmann, S. J. L. Billinge, N. Hur, and S. W. Cheong, *J. Phys.: Cond. Matter.* **16**, 7287 (2004).
- [20] W. Carrillo-Cabrera, H. Borrmann, M. Baenitz S.Paschen, F. Steglich, and Y. Grin, *J. Solid State Chem.* **178**, 715 (2005).
- [21] I. Zerec, A. Yaresko, P. Thalmeier, and Y. Grin, *Phys. Rev. B* **66**, 045115 (2002).
- [22] I. Zerec, W. Carrillo-Cabrera, V. Voevodin, J. Sichelschmidt, F. Steglich, Y. Grin, A. Yaresko, and S.-I. Kimura, *Phys. Rev. B* **72**, 045122 (2005).
- [23] T. Rachi, M. Kitajima, K. Kobayashi, F. Guo, T. Nakano, Y. Ikemoto, K. Kobayashi, and K. Tanigaki, *J. Chem. Phys.* **123**, 074503 (2005).
- [24] J. Tang, J. Xu, S. Heguri, H. Fukuoka, S. Yamanaka, K. Akai, and K. Tanigaki, *Phys. Rev. Lett.* **105**, 176402 (2010).
- [25] F. Kanetake, A. Harada, T. Rachi, H. Nagara, H. Mukuda, K. Kusakabe, Y. Kitaoka, N. Suzuki, K. Tanigaki, K. Itoh, and E. E. Haller, *J. Phys.: Conf. Ser.* **121**, 052011 (2008).
- [26] F. Kanetake, A. Harada, H. Mukuda, Y. Kitaoka, K. Tanigaki T.Rachi, K. Itoh, and E. E.Haller, *J. Phys. Soc. Jpn.* **78**, 104710 (2009).
- [27] H. Q. Yuan, F. M. Grosche, W. Carrillo-Cabrera, V. Pacheco, G. Sparn, M. Baenitz, U. Schwarz, Y. Grin, and F. Steglich, *Phys. Rev. B* **70**, 174512 (2004).
- [28] J.-H. Kim, N. L. Okamoto, K. Kishida, K. Tanaka, and H. Inui, *Acta Mater.* **54**, 2057 (2006).
- [29] J.-H. Kim, N. L. Okamoto, K. Kishida, K. Tanaka, and H. Inui, *J. Appl. Phys.* **102**, 034510 (2007).
- [30] J.-H. Kim, N. L. Okamoto, K. Kishida, K. Tanaka, and H. Inui, *J. Appl. Phys.* **102**, 094506 (2007).
- [31] H. Shimizu, T. Fukushima, T. Kume, S. Sasaki, H. Fukuoka, and S. Yamanaka, *J. Appl. Phys.* **101**, 113531 (2007).
- [32] J. Rodriguez-Carvajal, in *Applied Crystallography* (World Scientific, Singapore, 2001), pp. 30–36.
- [33] M. M. Koza, A. Leithe-Jasper, H. Rosner, W. Schnelle, H. Mutka, M. R. Johnson, and Y. Grin, *Phys. Rev. B* **89**, 014302 (2014).
- [34] M. M. Koza, M. R. Johnson, H. Mutka, M. Rotter, N. Nasir, A. Grytsiv, and P. Rogl, *Phys. Rev. B* **82**, 214301 (2010).
- [35] M. M. Bredov, B. A. Kotov, N. M. Okuneva, V. S. Oskotskii, and A. L. Shakh-Budagov, *Fizika Tverdogo Tela* **9**, 287 (1967) [*Sov. Phys. Solid State* **9**, 214 (1967)].



- [36] V. S. Oskotskii, *Fizika Tverdogo Tela* **9**, 550 (1967) [*Sov. Phys. Solid State* **9**, 420 (1967)].
- [37] G. Kresse and D. Joubert, *Phys. Rev. B* **59**, 1758 (1999).
- [38] J. P. Perdew, K. Burke, and M. Ernzerhof, *Phys. Rev. Lett.* **77**, 3865 (1996).
- [39] M. Methfessel and A. T. Paxton, *Phys. Rev. B* **40**, 3616 (1989).
- [40] H. J. Monkhorst and J. D. Pack, *Phys. Rev. B* **13**, 5188 (1976).
- [41] J. Hafner, *J. Comput. Chem.* **29**, 2044 (2008).
- [42] P. Vinet, J.-H. Rose, J. Ferrante, and J.-R. Smith, *J. Phys.: Condens. Matter* **1**, 1941 (1989).
- [43] K. Parlinski, Z.-Q. Li, and Y. Kawazoe, *Phys. Rev. Lett.* **78**, 4063 (1997).
- [44] M. M. Koza, L. Capogna, A. Leithe-Jasper, H. Rosner, W. Schnelle, H. Mutka, M. R. Johnson, C. Ritter, and Y. Grin, *Phys. Rev. B* **81**, 174302 (2010).
- [45] H. Euchner, S. Pailhès, L. T. K. Nguyen, W. Assmus, F. Ritter, A. Haghighirad, Y. Grin, S. Paschen, and M. de Boissieu, *Phys. Rev. B* **86**, 224303 (2012).
- [46] S. Pailhès, H. Euchner, V. M. Giordano, R. Debord, A. Assy, S. Gomes, A. Bosak, D. Machon, S. Paschen, and M. de Boissieu, *Phys. Rev. Lett.* **113**, 025506 (2014).
- [47] C. Candolfi, U. Aydemir, M. M. Koza, M. Baitinger, Yu. Grin, and F. Steglich, *J. Phys.: Cond. Mat.* **27**, 485401 (2015).
- [48] H. Euchner and A. Groß, *Chem. Mater.* **31**, 2571 (2019).
- [49] P.-F. Lory, S. Pailhès, V. M. Giordano, H. Euchner, H. D. Nguyen, R. Ramlau, H. Borrmann, M. Schmidt, M. Baitinger, M. Ikeda, P. Tomeš, M. Mihalkovič, C. Allio, M. R. Johnson, H. Schober, Y. Sidis, F. Bourdarot, L. P. Regnault, J. Ollivier, S. Paschen *et al.*, *Nat. Commun.* **8**, 491 (2017).
- [50] M. Christensen, A. B. Abrahamsen, N. B. Christensen, F. Juranyi, N. H. Andersen, K. Lefmann, J. Andreasson, C. R. H. Bahl, and B. B. Iversen, *Nat. Mater.* **7**, 811 (2008).
- [51] N. Melnychenko-Koblyuk, A. Grytsiv, L. Fornasari, H. Kaldarar, H. Michor, F. Röhrbacher, M. Koza, E. Royanian, E. Bauer, P. Rogl, *J. Phys.: Condens. Matter* **19**, 216223 (2007).
- [52] N. Melnychenko-Koblyuk, A. Grytsiv, P. Rogl, M. Rotter, E. Bauer, G. Durand, H. Kaldarar, R. Lackner, H. Michor, E. Royanian, M. Koza, and G. Giester, *Phys. Rev. B* **76**, 144118 (2007).
- [53] N. L. Okamoto, J.-H. Kim, K. Tanaka, and H. Inui, *Acta Mater.* **54**, 5519 (2006).
- [54] H. Fukuoka and S. Yamanaka, *J. Organomet. Chem.* **611**, 543 (2000).
- [55] T. F. Fässler and C. Kronseder, *Z. anorg. allg. Chem.* **624**, 561 (1998).
- [56] H. G. von Schnering, A. Zürn, J.-H. Chang, M. Baitinger, and Y. Grin, *Z. anorg. allg. Chem.* **633**, 1147 (2007).
- [57] T. Dahm and K. Ueda, *Phys. Rev. Lett.* **99**, 187003 (2007).
- [58] G. Lucazeau, *J. Raman Spectrosc.* **34**, 478 (2003).
- [59] G. A. Kourouklis and E. Anastassakis, *Phys. Status Solidi B* **152**, 89 (1989).
- [60] M. Falmbigl, G. Rogl, P. Rogl, M. Kriegisch, H. Müller, E. Bauer, M. Reinecker, and W. Schranz, *J. Appl. Phys.* **108**, 043529 (2010).
- [61] P. Toulemonde, D. Machon, A. San Miguel, and M. Amboage, *Phys. Rev. B* **83**, 134110 (2011).
- [62] A. San Miguel, P. Mélinon, D. Connétable, X. Blase, F. Tournus, E. Reny, S. Yamanaka, and J. P. Itié, *Phys. Rev. B* **65**, 054109 (2002).